química nova

Quim. Nova **2026**, *49*, e-20260089, 1-7
http://dx.doi.org/10.21577/0100-4042.20260089

Article

HIGH-ENTROPY NiFeCoCuW LAYERED DOUBLE HYDROXIDE PROMISES ADVANCED OXYGEN EVOLUTION IN ALKALINE WATER AND ALKALINE SEAWATER

Xinran Zang[a] and Jinxue Guo[a,*]

[a]Key Laboratory of Optic-electric Sensing and Analytical Chemistry for Life Science, Ministry of Education (MOE), Shandong Key Laboratory of Biochemical Analysis, College of Chemistry and Molecular Engineering, Qingdao University of Science and Technology, 266042 Qingdao, China

Received: 03/02/2026; accepted: 06/15/2026; published online: 06/23/2026

Water/seawater electrolysis is considered a pivotal technological route toward scalable and eco-friendly hydrogen generation and is recognized as a promising renewable alternative to conventional fossil fuels. Herein, high-entropy NiFeCoCuW layered double hydroxide (LDH) flower-like microspheres are fabricated via a facile one-pot hydrothermal strategy as efficient and stable oxygen evolution catalyst. An overpotential of only 118 mV is required for the as-prepared NiFeCoCuW-LDH catalyst to achieve a current density of 10 mA cm^{-2} in alkaline water, highlighting its exceptional oxygen evolution reaction (OER) performance. In alkaline seawater (1 M KOH + seawater), the catalyst achieves an OER overpotential of 122 mV at 10 mA cm^{-2}, while retaining satisfactory electrocatalytic activity. The NiFeCoCuW-LDH catalyst fabricated in this work not only possesses the superior catalytic activity and low cost of transition metal-based catalysts, but also exhibits the flexible electronic regulation capability and multimetal synergistic effects of high-entropy materials, which endows the catalyst with exceptional electrocatalytic performance.

Keywords: high-entropy; layered double hydroxide; oxygen evolution reaction; water splitting; seawater electrolysis.

INTRODUCTION

With the continuous advancement of the global industrialization process, the global demand for energy has been continuously escalating.[1] Consequently, the pursuit of energy sources that are not only cost-effective and renewable but also environmentally benign has become a matter of urgent priority.[2] High-purity hydrogen can be produced on a large scale through seawater electrolysis powered by renewable energy sources such as solar, wind, and hydropower, marking this approach as both promising and environmentally benign.[3-6] However, electrolytic oxygen evolution reaction (OER) involves a four-step electron-proton transfer process, and the slow reaction kinetics severely limit the overall efficiency of water splitting.[7] Currently, highly efficient OER catalysts are mainly dependent on platinum group metal-based catalysts (e.g., Pt/C, RuO_2, and IrO_2).[8-10] Nevertheless, the path to widespread commercialization is obstructed by two critical factors: the prohibitive cost and the inherent scarcity of noble metals in the Earth crust. Therefore, rational strategies need to be developed to explore high-efficiency catalysts suitable for seawater OER, thereby reducing overpotential and overcoming the fundamental technical hurdles in high-efficiency water electrolysis.

Among various non-noble metal catalysts, layered double hydroxides (LDH) stand out as promising candidates for enhancing the OER activity, owing to their unique two-dimensional layered structure, tunable metal composition in host layers and abundant surface hydroxyl active sites.[11,12] This distinctive layered structure enables the modulation of chemical composition and electronic structure, and facilitates the synergistic effect of multiple metal species toward water electrolysis. Traditional binary and ternary LDH still suffer from inherent drawbacks.[13,14] Their limited compositional tunability restricts the regulation of electronic structures. Additionally, high crystallinity leads to insufficient active sites. These materials also tend to detach and corrode during long-term electrolysis. Their catalytic performance is nearly saturated and fails to meet the requirements for high-current-density operation.

High-entropy materials have been recognized as a significant breakthrough in materials science in recent years.[15] Derived from high-entropy alloys, they have attracted widespread attention owing to their flexible regulation mechanism and abundant catalytic active sites.[16,17] High-entropy materials are composed of five or more metallic elements with near-equimolar ratios.[18-21] Through the utilization of high mixed entropy for stabilizing a single-phase solid solution structure, a homogeneous phase with unique properties is formed. The random distribution of various metallic elements leads to highly disordered atomic arrangements, thereby constructing structurally complex frameworks.[22] The resultant structural complexity generates abundant surface defects and vacancies, thereby increasing the number of accessible active sites.[23,24] The high-entropy structure not only enhances electrocatalytic performance through its unique architecture but also provides the stability necessary to preserve catalytic activity under demanding electrochemical conditions. Modification of LDH via introducing diverse metal cations into the host layers endows high-entropy effect, lattice distortion and metal synergism for catalyst. This strategy simultaneously regulates electronic structures, creates defective active sites and optimizes reaction adsorption energy, thereby improving the catalytic activity and stability of the catalysts.

High-entropy layered double hydroxides (HE-LDH) overcome the shortcomings of conventional binary and ternary LDHs and expand their application potential. Most reported HE-LDHs are mainly composed of low-valent transition metals. Their partially filled d orbitals facilitate the adsorption and activation of reactant molecules.[25,26] High-valence metals are rarely adopted in relevant systems. As a typical representative, high-valence tungsten can not only optimize the adsorption strength of reaction intermediates, but also form a strong covalent network with oxygen, which greatly

*e-mail: guojinxue@qust.edu.cn
Associate Editor handled this article: Sérgio A. M. de Lima

enhances the structural stability of catalysts.[27,28] HE-LDHs are mostly prepared by co-precipitation, stepwise doping and electrodeposition. These methods involve tedious procedures, easily produce impurities and only yield powdered samples. In contrast, the one-step hydrothermal method is simple to operate and ensures uniform metal distribution. It fully retains high-entropy lattice distortion and structural defects, and enables binder-free integrated electrodes with improved conductivity and stability.[29]

Herein, quinary high-entropy layered double hydroxide (LDH) microspheres are synthesized on nickel foam (NF) substrates via a facile one-step hydrothermal route. High-performance oxide electrocatalysts for water splitting fabricated by utilizing the polymetallic synergism and entropy stabilization effect of high-entropy LDH materials exhibit excellent OER catalytic activity. The differences in atomic radius and electronegativity among Ni, Fe, Co, Cu and W induce substantial lattice distortion, thus increasing catalytic active sites. Electronic coupling among five metallic components effectively modulates the electronic structure and forms robust metal-oxygen bonding network, which remarkably boosts catalytic efficiency and stability. The NiFeCoCuW-LDH catalyst demonstrates remarkable OER activity in alkaline electrolyte, requiring an overpotential of only 118 mV to reach 10 mA cm^{-2}, in addition to maintaining stable performance for over 20 h at an elevated current density of 200 mA cm^{-2}. Furthermore, the OER overpotential at 10 mA cm^{-2} was 122 mV in alkaline seawater, representing an increase of less than 3% compared with pure alkaline electrolyte systems. This indicates that impurity components in seawater exert a negligible impact on the OER performance of the catalyst, thus demonstrating its practical potential for application in seawater electrolysis.

EXPERIMENTAL

Chemicals and materials

Cobalt(II) nitrate hexahydrate ($Co(NO_3)_2.6H_2O$), nickel(II) nitrate hexahydrate ($Ni(NO_3)_2.6H_2O$), copper(II) nitrate trihydrate ($Cu(NO_3)_2.3H_2O$), iron(III) nitrate nonahydrate ($Fe(NO_3)_3.9H_2O$), sodium tungstate dihydrate (Na_2WO_4), urea ($CO(NH_2)_2$), ammonium fluoride (NH_4F), hydrochloric acid (HCl, 37 wt.%). Absolute ethanol was supplied from Aladdin. All chemicals were of analytical grade and were used as received without further purification. Nickel foam (NF, 2 × 2.5 cm) was ultrasonically cleaned in 10 wt.% HCl for 1 h for surface cleaning and hydrophilization, followed by rinsing with ethanol and deionized water sequentially.

Preparation of NiFeCoCuW-LDHs

The NiFeCoCuW-LDH catalyst was synthesized on a NF substrate via a hydrothermal method. $Co(NO_3)_2.6H_2O$, $Fe(NO_3)_3.9H_2O$, $Ni(NO_3)_2.6H_2O$, $Cu(NO_3)_2.3H_2O$, and Na_2WO_4 (3.5 mmol each) were added to 30 mL of deionized water and stirred for 1 h to obtain a homogeneous solution. Subsequently, 40 mmol of $CO(NH_2)_2$ and 15 mmol of NH_4F were added to the above solution in sequence and further stirred until complete dissolution. The resulting mixture was then transferred to a 40 mL Teflon-lined stainless-steel autoclave. After a piece of cleaned NF was immersed in the solution, the autoclave was sealed and heated at 120 °C for 10 h. The product was washed alternately with deionized water and ethanol for 3-5 times. The high-entropy NiFeCoCuW-LDH microspheres grown on NF were vacuum-dried at 60 °C for more than 12 h. Other control samples, including NiFeCoCu-LDH, NiFeCoW-LDH, NiFeCo-LDH, NiFeW-LDH, and NiW-LDH, were synthesized following the same procedure by removing the dosage of the corresponding metal salts.

Material characterization

The microstructure of NiFeCoCuW-LDH was examined using scanning electron microscope (SEM, JEOL JSM-7500F) and transmission electron microscope (TEM, JEOL JEM-F200). The surface chemical states and elemental composition were determined using X-ray photoelectron spectroscopy (XPS) on an RBD-upgraded PHI-5000C ESCA system (PerkinElmer). Powder X-ray diffraction (XRD) patterns were recorded on a Rigaku SmartLab SE diffractometer for crystallographic analysis.

Electrochemical measurements

All electrochemical measurements for OER were performed on a CHI760E electrochemical workstation equipped with a three-electrode system. In the three-electrode configuration, the as-prepared catalysts serve directly as the working electrodes. A platinum sheet functions as the counter electrode, with a Hg/HgO electrode acting as the reference electrode. The electrolytes used in the experiments included alkaline water (1 M KOH) and alkaline seawater (1 M KOH mixed with raw seawater). The alkaline seawater electrolyte was formulated by dissolving 1 mol of KOH in 1 L of raw seawater sourced directly from the Yellow Sea of China. Linear sweep voltammetry (LSV) at a scan rate of 5 mV s^{-1} was employed to probe the OER performance of the catalysts. All measured potentials were converted to the reversible hydrogen electrode (RHE) scale based on the Equation 1:

$$E_{RHE} = E_{Hg/HgO} + (0.098 + 0.059 \times pH)\ V \quad (1)$$

Tafel analysis was performed on the polarization curves based on the Equation 2, yielding the corresponding Tafel plots.

$$\eta = a + b\log(j) \quad (2)$$

where η is the overpotential, a is the constant related to the intrinsic catalytic activity of the material, b is the Tafel slope, j is the current density.

The electrochemical double-layer capacitance (C_{dl}) of NiFeCoCuW-LDH was determined from cyclic voltammetry (CV) curves recorded at different scan rates within a potential window free of faradaic reactions. Electrochemical impedance spectroscopy (EIS) was recorded at a constant overpotential of 100 mV across frequencies ranging from 0.1 Hz to 100 kHz. The stability was evaluated using chronopotentiometry and multi-step chronopotentiometry.

RESULTS AND DISCUSSION

The morphology of the synthesized NiFeCoCuW-LDH catalyst was characterized by SEM. Figure 1a shows the SEM image of the synthesized high-entropy NiFeCoCuW-LDH microspheres. The image clearly reveals that the sample exhibits a uniform microsphere morphology on the substrate, with diameters of approximately 7-8 μm and no significant agglomeration. The microsphere surface is formed by the oriented assembly of layered nanoplates, creating a richly wrinkled structure with exposed surface. The hybrization of five metallic elements within this high-entropy system does not disrupt the characteristic layered crystal structure of LDH; instead, elemental synergistic effects enhance the regularity of layered stacking. Efficient electron transport pathways are established within this three-dimensional architecture, which concurrently maximizes

the accessible surface area of the catalyst. Morphological differences are observed among catalysts with different metal compositions. As illustrated in Figure 1S (Supplementary Material), NiFeCoCu-LDH displays needle-like nanospheres. In contrast, NiFeCoW-LDH in Figure 2S (Supplementary Material) does not form complete spherical structures; instead, it presents as disordered nanosheet arrays decorated with irregular, coarse block-like particles on the surfaces and interfaces of the nanosheets.

As revealed by the TEM micrograph in Figure 1b, the LDHs adopt a spherical morphology composed of numerous stacked nanosheets. The magnified TEM image (Figure 1c) clearly shows a stacked sheet-like morphology, which is consistent with the typical morphological characteristics of layered double hydroxides.[30,31] Figure 1d shows the high-resolution TEM (HR-TEM) image of the NiFeCoCuW-LDH, in which the lattice fringes corresponding to the (101) and (012) planes of LDH are well detected, indicating the construction of high-entropy NiFeCoCuW-LDH. As shown by the energy dispersive spectroscopy (EDS) elemental mapping in Figure 1e, all metallic components and oxygen exhibit uniform spatial distribution within the layered double hydroxide (LDH) microsphere framework. This homogeneous elemental distribution is a hallmark of high-entropy systems, confirming the successful synthesis of this structure.

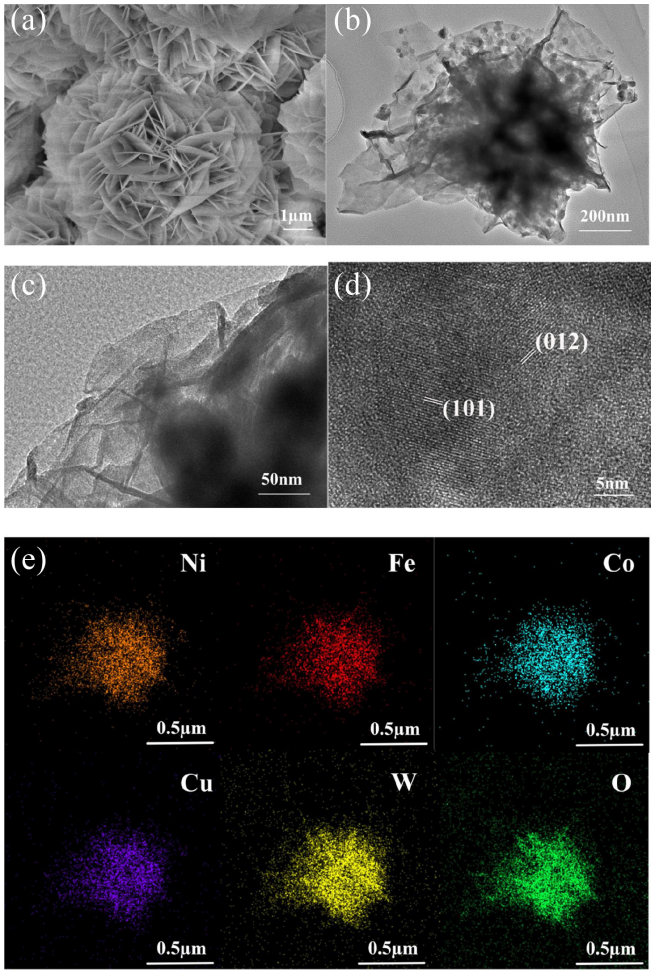

Figure 1. *(a) SEM; (b, c) TEM; (d) HR-TEM, and (e) EDS spectroscopy of NiFeCoCuW-LDH*

Figure 2 shows the XRD pattern of NiFeCoCuW-LDH and NiFeCoCu-LDH. It is clear that all diffraction peaks of NiFeCoCuW-LDH and NiFeCoCu-LDH are well consistent with NiFe-LDH,[32,33] indicating the successful formation of multimetallic LDHs. Varied ionic radii and charge states cause severe lattice distortion and stress in LDH structure, producing fine nanograins and XRD peak broadening. Multimetal doping lowers crystallinity, and amorphous phases account for the broad humps on the patterns.[34,35]

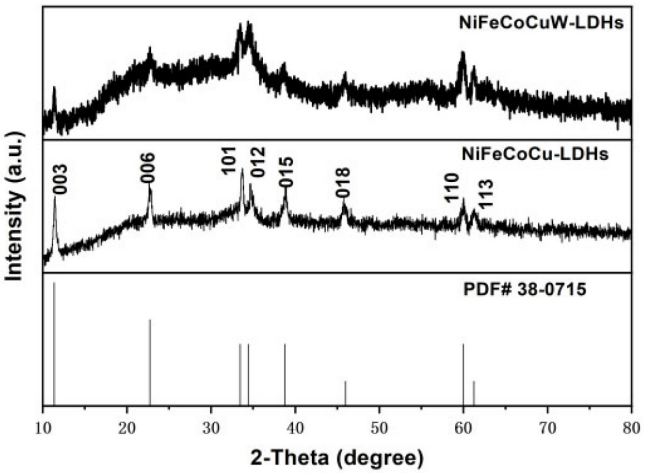

Figure 2. *XRD pattern of NiFeCoCuW-LDH*

The surface elemental composition and chemical states of NiFeCoCuW-LDH were characterized by XPS. Figure 3S (Supplementary Material) shows the full XPS spectrum, revealing characteristic peaks for Ni, Fe, Co, Cu, and W, accompanied by C 1s (284.8 eV) and O 1s (532.0 eV) peaks. In the O 1s spectrum, a shift toward higher binding energies is observed, which correlates with the addition of more metal ions and indicates enhanced covalent bonding between M–OH groups in Figure 4S (Supplementary Material). As shown in Figure 3a, two peaks appear at binding energies of 856.8 and 874.3 eV, corresponding to the $2p_{3/2}$ and $2p_{1/2}$ orbital signals of Ni^{2+}, respectively. This further confirms that Ni^{2+} is the primary chemical state of nickel in the sample. Distinct satellite peaks are observed at the high-binding-energy side of both the $2p_{3/2}$ (862.1 eV) and $2p_{1/2}$ (879.5 eV) lines.[36] The Fe 2p XPS spectrum (Figure 3b) exhibits a characteristic double peak near 710.0 eV, confirming the presence of Fe^0 and Fe^{2+} species. The peaks observed at 707.2 and 720.0 eV are attributed to the Fe $2p_{3/2}$ and Fe $2p_{1/2}$ orbitals of metallic Fe (Fe^0), whereas the signals located at 710.9 and 721.0 eV correspond to the Fe $2p_{3/2}$ and Fe $2p_{1/2}$ orbitals of Fe^{2+}, respectively.[37] In the Co 2p region of the high-resolution XPS spectra (Figure 3c), two primary peaks are observed at 781.2 and 797.1 eV, corresponding to the Co $2p_{3/2}$ and $2p_{1/2}$ orbitals of Co^{2+}. Additionally, their satellite features appear at 786.2 and 803.6 eV, respectively.[38] As shown in Figure 3d, Cu^{2+} species are detected at binding energies of 934.8 eV (Cu $2p_{3/2}$) and 954.8 eV (Cu $2p_{1/2}$), indicating that Cu primarily exists in an oxidized state within the LDH layers.[39,40] Additionally, the W 4f XPS spectrum (Figure 3e) exhibits distinct peaks at 35.2 eV (W $4f_{7/2}$) and 37.7 eV (W $4f_{5/2}$), alongside a characteristic signal for highly oxidized W^{6+}.[41] This confirms the successful incorporation of W^{6+} into the electrocatalyst NiFeCoCuW-LDH. Analysis of the XPS spectrum reveals that Ni, Fe, Co, and Cu predominantly exist as divalent oxides (Ni^{2+}, Fe^{2+}, Co^{2+}, Cu^{2+}) within layered hydroxides, while W is uniformly dispersed in the layered structure as highly oxidized W^{6+} hydroxide. This structure facilitates electron regulation and enhances structural stability, thereby boosting the OER activity of the catalyst.

The OER activity of the high-entropy LDH electrocatalysts was first evaluated in a conventional three-electrode system using 1.0 M KOH as the electrolyte. Figure 4a presents the LSV curves at a scan rate of 5 mV s^{-1}, where the superior electrocatalytic

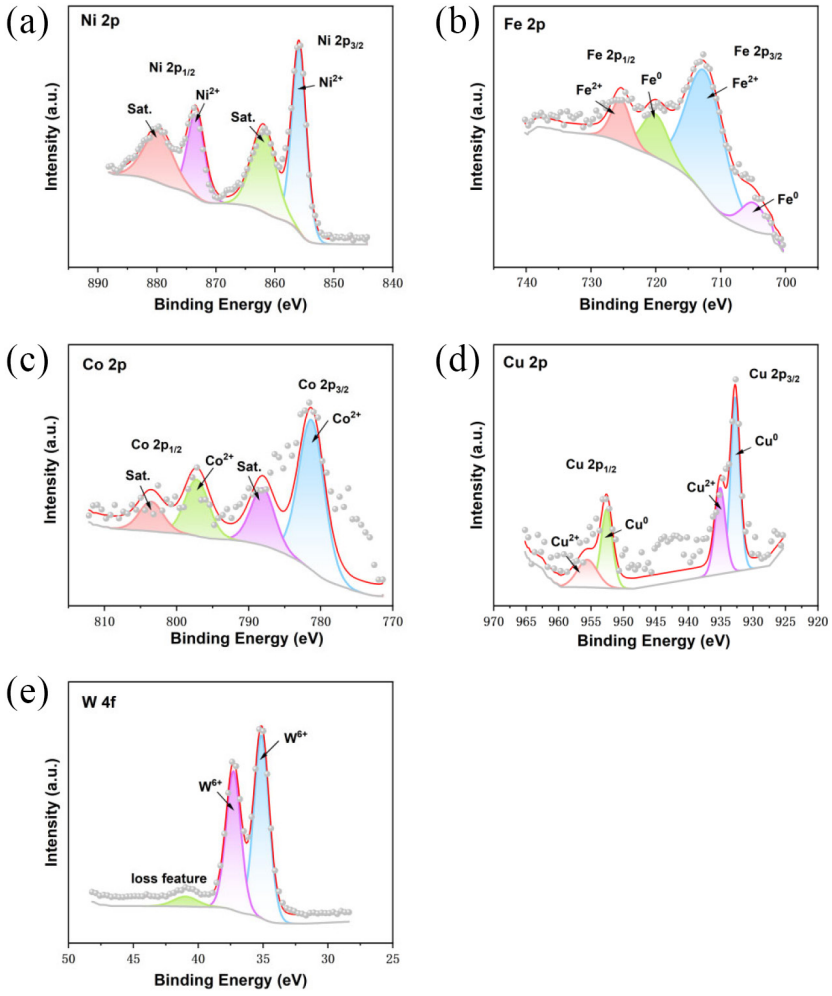

Figure 3. *(a) Ni 2p; (b) Fe 2p; (c) Co 2p; (d) Cu 2p, and (e) W 3f XPS spectrum of NiFeCoCuW-LDH*

activity of NiFeCoCuW-LDH is clearly observed. An exceptionally low overpotential of only 118 mV is required for the OER at a current density of 10 mA cm^{-2}, which is significantly lower than those of the control samples, namely NiFeCoCu-LDH (141 mV), NiFeCoW-LDH (209 mV), NiFeCo-LDH (200 mV), NiFeW-LDH (239 mV), and NiW-LDH (348 mV) (Figure 4b). Furthermore, it also outperforms the noble metal OER catalyst IrO_2 (253 mV). Even at a high current density of 100 mA cm^{-2}, the quinary high-entropy LDH sample still maintains the lowest overpotential, demonstrating superior OER catalytic performance across the entire current density range. Table 1S (Supplementary Material) compares this catalyst with similar catalysts reported in recent literature,[42-50] clearly showing that NiFeCoCuW-LDH exhibits a lower overpotential toward the oxygen evolution reaction in alkaline media. The above analysis indicates that the synergistic effect among the five metals (Ni, Fe, Co, Cu, and W) effectively reduces the adsorption energy barrier of OER intermediates, highlighting the promotional role of the high-entropy effect in electrocatalysis. The Tafel plots derived from the LSV curves, which reflect the catalytic reaction kinetics of the different electrocatalysts, are shown in Figure 4c. The smallest Tafel slope of 90.18 mV dec^{-1} is observed for NiFeCoCuW-LDH, suggesting the most favorable OER kinetics among all the samples. This small slope indicates a higher charge transfer coefficient and a faster oxygen evolution rate, an enhancement that can most likely be attributed to the unique high-entropy effect.

To investigate the interfacial charge transfer kinetics, EIS measurements were conducted, providing the charge transfer resistance (Rct) values for the high-entropy hydroxide catalysts. Equivalent circuit fitting of the EIS data (Figure 4d) demonstrates that NiFeCoCuW-LDH possess the lowest charge transfer resistance (0.51 Ω), indicating that high-entropy endows superior electrical conductivity and faster electron transfer kinetics. This result, which aligns well with the Tafel slope analysis, accounts for its enhanced OER catalytic activity. The electrochemical surface area (ECSA) of various catalysts is estimated by calculating the C_{dl} from the current response in the non-Faradaic region of the CV curves, obtained from CV tests conducted at various scan rates (10-120 mV s^{-1}). As shown in Figure 4e, the NiFeCoCuW-LDH catalyst exhibits a higher C_{dl} (21.79 mF cm^{-2}) than other samples, indicating more exposed catalytic active sites that derived from high-entropy effect.

Additionally, the stability of the catalyst was evaluated using chronopotentiometric and multi-step chronopotentiometric measurements. Figure 4f shows that NiFeCoCuW-LDH exhibited no significant change in corresponding voltage after 20 h of electrochemical testing at a current density of 200 mA cm^{-2}, indicating that the strong covalent bonds formed with oxygen due to multimetal interactions and the presence of W^{6+} significantly enhance catalyst stability at high current densities. The multi-step chronopotentiometric curve shown in Figure 4g indicates that the potential stabilized at 1.45 V and remained essentially unchanged over 500 s at 20 mA cm^{-2}. Similar behavior is observed at other current densities, indicating that this catalyst possesses excellent electron transfer capability, mechanical robustness, and electrical conductivity.

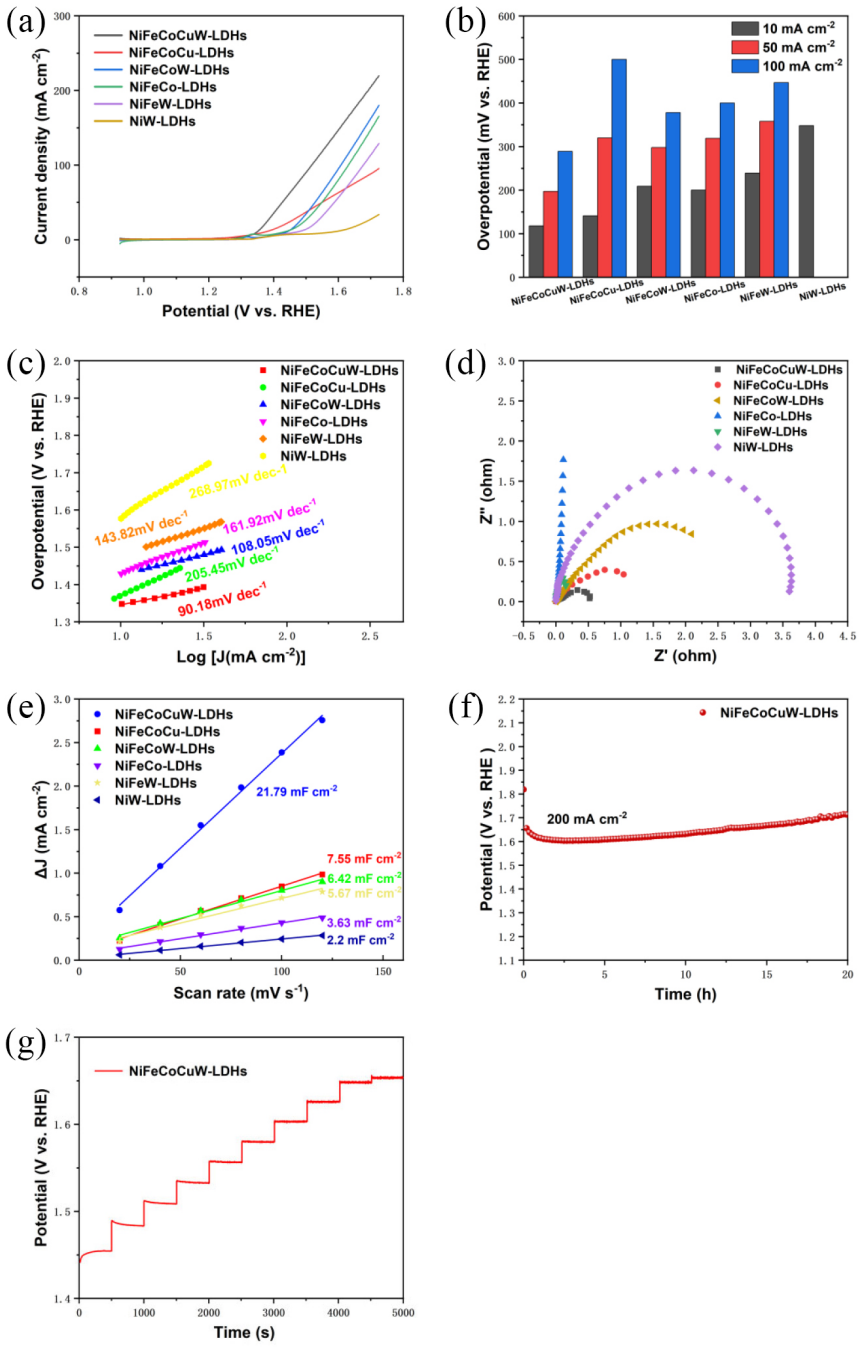

Figure 4. *Electrocatalysis OER tests of NiFeCoCuW-LDH, NiFeCoCu-LDH, NiFeCoW-LDH, NiFeCo-LDH, NiFeW-LDH, and NiW-LDH in 1.0 M KOH. (a) Polarization curves; (b) overpotentials at different current densities; (c) Tafel plots; (d) electrochemical impedance spectra; (e) capacitive currents as a function of scan rate; (f) chronopotentiometry test at 200 mA cm^{-2} for 20 h, and (g) multi-step chronopotentiostatic test at current densities ranging from 20 to 200 mA cm^{-2}*

Due to the outstanding OER electrocatalytic performance of the NiFeCoCuW-LDH catalyst in alkaline solution (1 M KOH), electrochemical tests were conducted using alkaline seawater (1 M KOH + seawater) as the electrolyte. The results demonstrate that the high-entropy catalyst maintains good OER activity in alkaline seawater, indicating its promising potential for seawater electrolysis. As shown in Figure 5a, the LSV polarization curves revels that the overpotentials of the NiFeCoCuW-LDH catalyst at 10 and 50 mA cm^{-2} are 122 and 255 mV, respectively, representing an increase of less than 3% compared to the overpotentials measured in pure 1 M KOH alkaline solution.

The Tafel slope plot (Figure 5b) reveals that this sample exhibits an extremely low Tafel slope of 29.4 mV dec^{-1} in alkaline seawater, which is even lower than that measured in alkaline electrolyte. This indicates that the abundant ions in seawater accelerate electron transfer during the reaction, demonstrating superior electrocatalytic activity. As observed from the EIS curves (Figure 5c), the NiFeCoCuW-LDH catalyst exhibits the smallest curve radius and the lowest reaction resistance, which should be due to the improved charge transfer of high-entropy effect. As shown in Figure 5d, this sample exhibits a high C_{dl} value of 10.9 mF cm^{-2}, indicating that alkaline seawater has minimal impact on its catalytic active sites. The high-entropy effect endows the catalyst with a significant number of lattice distortions or defects for the oxygen evolution reaction in alkaline seawater. Figures 5e and 5f show the chronopotentiometric curves recorded at a current density of

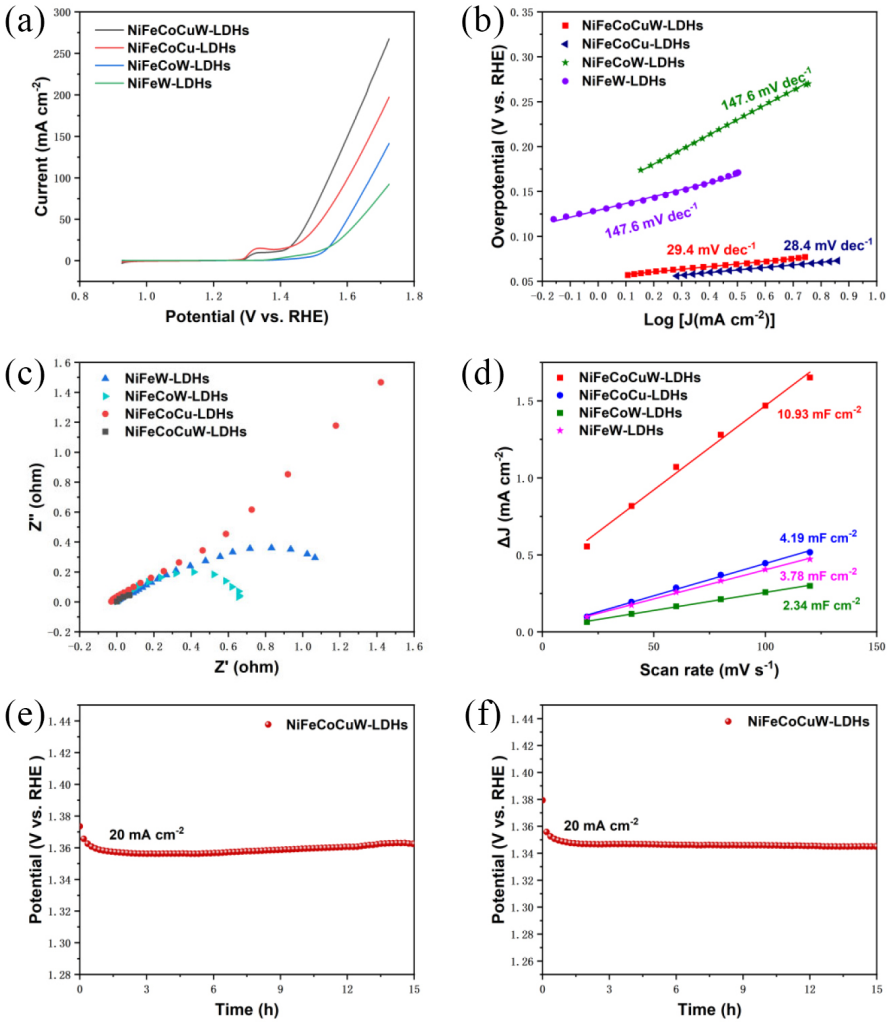

Figure 5. *Electrocatalysis OER tests of NiFeCoCuW-LDH, NiFeCoCu-LDH, NiFeCoW-LDH, and NiFeW-LDH in 1.0 M KOH + seawater. (a) Polarization curves; (b) Tafel plots; (c) electrochemical impedance spectra; (d) capacitive currents as a function of scan rate. Chronopotentiometric curves at 20 mA cm^{-2} for 15 h test in (e) alkaline solution and (f) alkaline seawater*

20 mA cm^{-2} over 15 h in alkaline solution and alkaline seawater, respectively. The comparison indicates that seawater shows a negligible impact on the catalyst stability. This demonstrates that NiFeCoCuW-LDH significantly enhances the M–O bond energy, leading to long-term stable catalytic performance.

CONCLUSIONS

In summary, this study reports the synthesis of flower-shaped microsphere catalysts composed of high-entropy quinary layered double hydroxides using a single-step hydrothermal method. This catalyst exhibits outstanding catalytic performance for the OER in both alkaline water and alkaline seawater. NiFeCoCuW-LDH possess the following key characteristics:

(*i*) The hydrothermal process achieves atomically uniform dispersion of five metals on the LDH layers. The nanosheet-assembled microsphere structure maximizes the specific surface area of the material, providing ample physical reaction sites for OER and enhancing electron transport and mass diffusion rates.

(*ii*) Due to varying metal atomic sizes and disordered atomic arrangements, high entropy effects are created, such as larger structural defects and lattice distortions, which increases the number of sites capable of contacting the electrolyte and participating in the catalytic reaction.

(*iii*) The five transition metals not only optimize the oxygen adsorption strength during the OER, but also readily forms strong covalent bonds with oxygen, thereby effectively preserving the structural integrity of the layered LDH framework and guaranteeing the electrochemical stability of the catalyst. Leveraging these advantages, NiFeCoCuW-LDH exhibits a low overpotential of 118 mV (at a current density of 10 mA cm^{-2}) and 197 mV (at 50 mA cm^{-2}) in alkaline solutions. When tested in alkaline seawater, it exhibits an overpotential of just 122 mV at 10 mA cm^{-2}, confirming its high activity and stability for the OER. Overall, this study provides a novel approach for optimizing electrocatalysts based on high-entropy hydroxides for water electrolysis, paving the way for their potential application in seawater electrolysis.

SUPPLEMENTARY MATERIAL

Some images of the systems used in this work are available in http://quimicanova.sbq.org.br, as a PDF file, with free access.

DATA AVAILABILITY STATEMENT

All data generated or analyzed during this study are included in this published article. Additional data may be requested from the corresponding authors.

ACKNOWLEDGMENTS

We thank for the financial support from Shandong Provincial Natural Science Foundation (ZR2019MEM035).

REFERENCES

1. Wen, N.; Jiao, X. L.; Xia, Y. G.; Chen, D. R.; *Mater. Chem. Front.* **2023**, *7*, 4833. [Crossref]
2. Song, J.; Zhu, Y. T.; Liang, D. X.; Cheng, Q.; Yao, D. W.; Bao, W. H.; *E3S Web Conf.* **2021**, *233*, 01083. [Crossref]
3. Lu, Z. S.; Yang, H.; Qi, G. C.; Liu, Q.; Feng, L. G.; Zhang, H.; Luo, J.; Liu, X. J.; *Small* **2024**, *20*, 2308841. [Crossref]
4. Liao, L. L.; Li, D. Y.; Zhang, Y.; Zhang, Y.; Yu, F.; Yang, L.; Wang, X. Z.; Tang, D. S.; Zhou, H. Q.; *Adv. Mater.* **2024**, *36*, 2405852. [Crossref]
5. Guo, J. M.; Lang, K.; Yang, X. H.; Yang, R.; Ru, M. X.; Xiao, X. D.; Meng, H. Y.; Jiang, B. J.; *Int. J. Hydrogen Energy* **2025**, *130*, 373. [Crossref]
6. Wu, L. G.; Yuan, J. H.; Wang, Y. M.; Chen, Z. L.; Ma, X. W.; Li, H.; Guo, Y. H.; Weng, S.; Bi, Q. Y.; Fan, J. C.; Li, G. S.; Hao, W. J.; *ACS Sustainable Chem. Eng.* **2025**, *13*, 20042. [Crossref]
7. Xu, Z. K.; Qi, Z. R.; *Small* **2021**, *17*, 2100129. [Crossref]
8. Wang, C.; Jin, L. J.; Shang, H. Y.; Xu, H.; Shiraishi, Y.; Du, Y. K.; *Chin. Chem. Lett.* **2021**, *32*, 2108. [Crossref]
9. Liu, P. F.; Zhang, R. Z.; Li, X. H.; Cui, H. L.; *Int. J. Hydrogen Energy* **2025**, *101*, 212. [Crossref]
10. Huang, R. X.; Zhang, Z. P.; Sang, C. C.; Gao, W. T.; Bai, Y. M.; Huang, Y. H.; Shi, Y. X.; Li, Y. H.; Sun, L. G.; Wang, C.; Gu, J.; Yu, T.; *Green Chem.* **2026**, *28*, 2077. [Crossref]
11. Gaur, A.; Sharma, J.; Lim, D. H.; Lee, H. I.; Han, H.; *ChemCatChem* **2025**, *17*, e202401584. [Crossref]
12. Hameed, A.; Batool, M.; Liu, Z. Y.; Nadeem, M. A.; Jin, R. C.; *ACS Energy Lett.* **2022**, *7*, 3311. [Crossref]
13. Chen, Z. X.; Wang, D.; Wang, F. Y.; Wang, W. C.; Dong, C. P.; Zhou, Y. Y.; Shan, X. L.; Chen, Z. D.; *Catal. Lett.* **2026**, *156*, 58. [Crossref]
14. Silva, A.; Bomfim, J.; Tomaso, L.; de Paiva, J.; Senra, J.; Malta, L.; Carvalho, N.; *J. Electroanal. Chem.* **2025**, *995*, 119298. [Crossref]
15. Li, X. Y.; Song, J.; Ma, J.; Wang, J.; *Adv. Funct. Mater.* **2026**, e22273. [Crossref]
16. Anantharaj, S.; Karthick, K.; Kundu, S.; *Mater. Today Energy* **2017**, *6*, 1. [Crossref]
17. Zhang, W.; Zhang, X. Y.; Song, Y.; Gao, F.; Zhang, Y. P.; *Chem. Commun.* **2025**, *61*, 7532. [Crossref]
18. Zhang, Q.; Zhang, S. S.; Luo, Y.; Liu, Q.; Luo, J.; Chu, P. K.; Liu, X. J.; *APL Mater.* **2022**, *10*, 070701. [Crossref]
19. Xiang, X. H.; Zheng, X. H.; Qi, M. R.; Xue, C. Y.; Zhong, L. G.; Yuan, Y. S.; Qin, M. A.; *Mater. Rep.* **2022**, *36*, 57. [Crossref]
20. Yuan, W. P.; Cheng, D. G.; Gui, Z. D.; Hao, L. Y.; Min, S. S.; Ming, F. S.; *Mater. Rep.* **2024**, *38*, 83. [Crossref]
21. Zeng, L. Y.; Li, K.; Li, L. F.; Yu, P. F.; Wang, K. W.; Chen, R.; Zhang, C.; Xiang, Z. C.; Shi, L.; Zhang, Y. W.; Jiang, K. Y.; Luo, H. X.; *Chin. Sci. Bull.* **2024**, *69*, 2951. [Crossref]
22. Wu, Y.; Li, Z.; Feng, H.; He, S.; *Materials* **2022**, *15*, 3992. [Crossref]
23. Liu, Y. F.; Ye, C. C.; Chen, L.; Fan, J. B.; Liu, C.; Xue, L.; Sun, J. W.; Zhang, W. Q.; Wang, X.; Xiong, P.; Zhu, J. W.; *Adv. Funct. Mater.* **2024**, *34*, 2314820. [Crossref]
24. Wang, Z. J.; Liu, C. T.; Dou, P.; *Phys. Rev. Mater.* **2017**, *1*, 043601. [Crossref]
25. Zhang, T. Y.; Zhu, Y. C.; Zhou, X. T.; Zhang, J. L.; Guo, D. Y.; Zhou, L. Y.; Chen, X.; Wang, S.; *Chem. Eng. J.* **2025**, *521*, 166512. [Crossref]
26. Seki, Y.; Wakabayashi, Y. K.; Takeda, T.; Inagaki, K.; Fujimori, S. I.; Takeda, Y.; Fujimori, A.; Taniyasu, Y.; Yamamoto, H.; Krockenberger, Y.; Tanaka, M.; Kobayashi, M.; *Phys. Rev. Lett.* **2025**, *135*, 046402. [Crossref]
27. Tang, T. T.; Cao, Y. T.; Li, M.; Cui, S.; Wu, Y.; Yu, Z. Z.; Cui, W.; Zhao, H.; *Chem. Eng. Sci.* **2026**, *320*, 122672. [Crossref]
28. Sun, Y.; Yang, F.; Sun, S. Y.; Wei, K. X.; Wang, Y.; Ma, G.; An, J. P.; Yuan, J. W.; Zhao, M. T.; Liu, J. H.; Liu, H. C.; Li, Y. F.; *J. Colloid Interface Sci.* **2025**, *684*, 1. [Crossref]
29. Gao, C. H.; Duan, G. G.; Han, X. S.; Shi, Q.; Huang, Y.; Zhang, C. M.; He, S. J.; Jiang, S. H.; *Coord. Chem. Rev.* **2026**, *550*, 217445. [Crossref]
30. Madhavan, J.; Arumugam, D.; Chinnasamy, S.; Karthikesan, P.; Sharan, H.; Ramasamy, S.; Balakrishnan, P.; Mani, A.; *Fuel* **2026**, *417*, 138613. [Crossref]
31. Zhou, J. Q.; Duan, R. X.; Xiao, J. Y.; Zhang, S. Y.; Huang, C. Q.; Xie, Y. L.; Yang, L.; Liu, Y.; Du, Y.; Yu, L.; Yu, Y.; *J. Energy Chem.* **2026**, *114*, 808. [Crossref]
32. Jia, Y.; Zhang, L. Z.; Gao, G. P.; Chen, H.; Wang, B.; Zhou, J. Z.; Soo, M. T.; Hong, M.; Yan, X. C.; Qian, G. R.; Zou, J.; Du, A. J.; Yao, X. D.; *Adv. Mater.* **2017**, *29*, 1700017. [Crossref]
33. Zhang, H. J.; Li, X. P.; Hähnel, A.; Naumann, V.; Lin, C.; Azimi, S.; Schweizer, S. L.; Maijenburg, A. W.; Wehrspohn, R. B.; *Adv. Funct. Mater.* **2018**, *28*, 1706847. [Crossref]
34. Chu, X.; Wang, T.; Wang, H.; Du, B.; Guo, G.; Zhou, Y.; Dong, X.; *J. Alloys Compd.* **2024**, *1003*, 175584. [Crossref]
35. Wang, Z. L.; Li, C.; Chen, C. C.; Huang, G. Y.; Zhu, H. B.; *Appl. Catal., B* **2026**, *386*, 126382. [Crossref]
36. Cai, Y. Q.; Li, Q. Y.; Zhao, H. Q.; Wan, Q.; Li, S. F.; Zhou, Y. J.; Liu, F. M.; Dou, X. X.; He, J. S.; Li, K. Y.; Yan, L. J.; *Appl. Surf. Sci.* **2025**, *713*, 164323. [Crossref]
37. Zhang, F. M.; Ublekov, F. L.; Li, Y.; Zhao, W. B.; Liu, S. C.; Liu, F. M.; Li, J. H.; Yu, M.; Cheng, F. Y.; *Chem. Commun.* **2026**, *62*, 4764. [Crossref]
38. Abedi, P.; Farhadi, K.; Hosseini, S. A.; Hooshyari, K.; *J. Environ. Chem. Eng.* **2026**, *14*, 120697. [Crossref]
39. Ma, X. L.; Li, X. M.; Jagadale, A. D.; Hao, X. G.; Abudula, A.; Guan, G. Q.; *Int. J. Hydrogen Energy* **2016**, *41*, 14553. [Crossref]
40. Cheng, S. Y.; Wang, T.; Kou, J. W.; Cheng, F. Q.; Song, H. P.; Zhao, H. Z.; *Fuel* **2024**, *361*, 130711. [Crossref]
41. Ding, L.; Li, K.; Xie, Z. Q.; Yang, G. Q.; Yu, S. L.; Wang, W. T.; Cullen, D. A.; Yu, H. R.; Zhang, F. Y.; *Electrochim. Acta* **2021**, *395*, 139199. [Crossref]
42. Wondimu, T. H.; Leung, P.; Zuo, Y.; Shah, A.; Liao, Q.; *J. Power Sources* **2025**, *640*, 236665. [Crossref]
43. Wu, H.; Zhang, J. F.; Lu, Q.; Li, Y. J.; Jiang, R.; Liu, Y.; Zheng, X. R.; Zhao, N. Q.; Li, J.; Deng, Y. D.; Hu, W. B.; *ACS Appl. Mater. Interfaces* **2023**, *15*, 38423. [Crossref]
44. Peng, K.; Cui, P.; Miao, F.; *Int. J. Hydrogen Energy* **2025**, *158*, 150578. [Crossref]
45. Yue, X. Y.; Liang, H. Y.; Zhang, Y. S.; Zhou, Y. Q.; Wang, J. J.; Xie, Z. K.; Yang, P.; Ma, Y. F.; Li, X. M.; *Appl. Catal., A* **2025**, *704*, 120408. [Crossref]
46. Zhong, X. H.; Wang, H. Y.; Zhang, C.; Wang, W. H.; Nelson, C. T.; He, X. Q.; Sun, Q. Q.; Gibson, B. G.; Neupane, M.; Deng, B. L.; Liu, M. J.; Yang, Y. C.; *Adv. Funct. Mater.* **2025**, *35*, e18240. [Crossref]
47. Wang, F. Q.; Li, Y.; Zhang, Y. Y.; Zheng, X. R.; Liang, L. M.; Huang, M. J.; Deng, Y. D.; Zheng, S. J.; Liu, H.; *ACS Catal.* **2025**, *15*, 11970. [Crossref]
48. Wang, F. Q.; Pan, W. L.; Li, Y.; Liang, L. M.; Uchimoto, Y.; Hao, Q. Y.; Liu, H.; Zheng, S. J.; *ACS Sustainable Chem. Eng.* **2025**, *13*, 5953. [Crossref]
49. Liu, F.; Fan, M.; Yan, H.; Wang, Z.; Song, J.; Wang, H.; Ren, J.; *Catalysts* **2024**, *14*, 502. [Crossref]
50. Mehravaran, M.; Asadpour-Zeynali, K.; *Heliyon* **2025**, *11*, e42072. [Crossref]